

# Development and Performance of Ultra-High Energy Resolution Dreamline Beamline at SSRF\*

Zhen-Hua Chen<sup>†,1</sup>, Ying Zou<sup>†,1</sup>, Jun-Qin Li<sup>1</sup>, Fang-Yuan Zhu<sup>1</sup>, Yi-Wei Cheng<sup>1</sup>, Yao-Bo Huang<sup>1,†</sup>, Yong Wang<sup>1,‡</sup> and Ren-zhong Tai<sup>1,§</sup>

<sup>1</sup>Shanghai Synchrotron Radiation Facility, Shanghai Advanced Research Institute,  
Chinese Academy of Sciences, Shanghai 201204, China.

The ultrahigh-energy-resolution soft X-ray beamline, "Dreamline," at the Shanghai Synchrotron Radiation Facility (SSRF), has been successfully constructed and is now fully operational for conducting angle-resolved photoemission spectroscopy (ARPES) and photoelectron emission microscopy (PEEM) experiments. Both branches of the beamline utilize a sophisticated plane-grating monochromator equipped with four variable-line-spacing gratings, enabling it to span an impressive energy range of 20–2000 eV. To achieve optimal performance in photon flux, energy-resolving power, and focus spot size, extensive optical optimization has been carried out. Notably, the energy resolution at the ARPES sample positions has been measured to be an impressive 17.2 meV at 867.1 eV, setting a new benchmark for the highest resolution capability within this energy range among similar international facilities. Furthermore, under the  $4\sigma$  opening of the white light slit, the full energy range flux of double undulator exceeds  $10^{12}$  photons per second per 0.01% bandwidth (phs/s/0.01%BW) below 800 eV when selecting the appropriate grating, while the flux across the full energy range remains above  $10^{11}$  phs/s/0.01%BW. The "Dreamline" beamline boasts a wide energy range support coupled with ultra-high energy resolution, making it an invaluable tool for advancing research in quantum materials.

Keywords: Synchrotron radiation, Beamline, High resolution, Monochromator, SSRF

## I. INTRODUCTION

Quantum materials, such as superconductors,[1] topological materials,[2] heavy fermion systems,[3] and magnetic materials,[4, 5] have emerged as significant research frontier due to their exotic quantum properties and revolutionary technological potential. Understanding these materials demands multidimensional characterization, where band structure analysis (revealing the distribution and motion state of electrons) is crucial for understanding the physical properties of these materials.[6] This analysis establishes quantitative connections between microscopic electronic behavior (e.g., electron correlations, spin-orbit coupling) and macroscopic properties—including electron-paring in superconductors[6,7], surface-protected topological effects[8], and magnetically ordered configurations[9,10]. Notably, strong correlations and competing interactions in these systems often defy conventional theoretical descriptions, necessitating experimental techniques capable of resolving subtle electronic structures with both spatial and energy precision.

Two photoelectron-based spectroscopies, Angle-resolved photoemission spectroscopy (ARPES) [11] and photoemission electron microscopy (PEEM) [12] are essential tools for studying quantum materials. ARPES enables direct momentum-space visualization of band structures through high-energy/angle-resolution spectroscopy, offering unprecedented insights into Cooper pair formation mechanisms in superconductors[13], spin polarization in spintronic materials [14], Fermi surface topology in topological insulators[15]

and strong electron correlation in diluted semiconductors[16]. Notably, for conventional ARPES, where vacuum ultraviolet (VUV) light is used, the escape depth of photoelectrons in solids is limited to a just a few angstroms [17], makes it ideal for probing surface-dominated systems like quasi-2D materials (Cuprate and Iron based high-temperature superconductors, etc). Complementarily, PEEM integrates spectroscopic data with nanoscale imaging[18], allowing real-time mapping of surface state dynamics and interface effects—critical for understanding spintronic materials.

While VUV-ARPES/PEEM dominate surface-sensitive studies, bulk property characterization requires deeper probing depths. Soft X-ray-based ARPES overcomes this limitation through synchrotron radiation excitation, achieving penetration depths exceeding Nano-meters compared to traditional VUV ARPES[11]. However, Soft-X ray ARPES meets the challenge for achieving high resolution, not only because of higher photon energy, but also due to reduction of beam flux and cross-section normally in this energy range comparing with VUV. For example, the optimal energy resolution at the ADDRESS beamline [19] is only 30 meV@ 900 eV. To meet the demand of high energy resolution in the soft X-ray region for band structure studies, a new soft X-ray beamline, "Dreamline," has been designed [20] and constructed at the Shanghai Synchrotron Radiation Facility (SSRF). It operates in 20-2000 eV energy range with record energy resolution of 17.2 meV at 867 eV [20]. The Dreamline beamline uniquely combines synchrotron advantages (with insertion device)—high brightness, wide tunability, and polarization control—with advanced real/momentum space detection systems. This state-of-the-art facility has enabled groundbreaking discoveries, including the experimental observation of Weyl fermions in TaAs [21], the three component fermions in MoP [22], the unconventional chiral fermions in CoSi [23], spin splitting in an antiferromagnet [4], and several of other notable accomplishments. Its design has catalyzed multidis-

\* The work is supported by the Shanghai Municipal Science and Technology Major Project. †The authors contributed equally to this work.

† Corresponding author, Yao-Bo Huang, [huangyaobo@sari.ac.cn](mailto:huangyaobo@sari.ac.cn)

‡ Corresponding author, Yong Wang, [wangyong@sari.ac.cn](mailto:wangyong@sari.ac.cn)

§ Corresponding author, Ren-Zhong Tai, [tairz@sari.ac.cn](mailto:tairz@sari.ac.cn)

65 ciplinary collaborations, producing several high-impact pub-  
 66 lications since commissioning in 2015.

## 67 II. BEAMLINE OPTICAL ARCHITECTURE

68 SSRF is the Chinese first 3rd-generation synchrotron,  
 69 which boasts an electron energy of 3.5 GeV and a low  
 70 emittance of 3.9 nm rad.[24-29] The Dreamline, developed  
 71 with the aim of providing an ultra-high-resolution beam-  
 72 line, bridges the VUV and soft X-ray regimes (20-2000 eV)  
 73 through a innovated two APPLE II-type elliptically polar-  
 74 ized undulators (EPU) (where EPU148 is used for 20-300 eV  
 75 and EPU58 for 200-2000 eV). This dual-source configura-  
 76 tion ensures continuous coverage with strategic overlap (200-  
 77 300 eV), enabling seamless transitions between surface-state  
 78 probing (with low photon energy) and bulk property analy-  
 79 sis capabilities (with high photon energy), based on the pen-  
 80 etration depth study result of electrons in solids. Notably,  
 81 the undulators support dynamic polarization switching among  
 82 linear horizontal/vertical and left/right circular polarizations,  
 83 facilitating orbital symmetry studies through selection rule  
 84 analysis in the process of photoemission – critical for com-  
 85 plex multi-orbital behavior inherent in quantum materials,  
 86 like the iron-based superconductors iron-based superconduct-  
 87 tors.[30]

88 The optical design of the beamline has been optimized  
 89 specifically for the ARPES branch, as it represents one of  
 90 the most demanding experiment needs. The beamline optical  
 91 layout (Fig. 1a) prioritizes high-energy resolution through  
 92 minimized non-planar components upstream of the exit slit.  
 93 A plane mirror (M1) with 1.2° incidence angle serves dual  
 94 purposes: heat load management via integrated water cool-  
 95 ing and harmonic suppression. The angle of incidence on  
 96 M1 was carefully selected striking a delicate balance between  
 97 ensuring high reflectivity at high photon energies and filter-  
 98 ing the power transmitted to downstream optical components.  
 99 To mitigate the potential impact of the significant absorbed  
 100 power, which can reach a maximum of 1500W, an integrated  
 101 water-cooling system has been implemented for M1.

102 The primary element of beamline is a vertically dis-  
 103 persing variable-line-spacing plane-grating monochromator  
 104 (VLS-PGM) [31], which is also capable of achieving verti-  
 105 cal beam focusing towards the exit slits. The VLS-PGM  
 106 is equipped with four holographically ruled gratings: a low  
 107 energy resolution grating (LEG), a middle energy resolution  
 108 grating (MEG), a high energy resolution grating (HEG) and a  
 109 very high resolution energy grating (VEG) with center groov-  
 110 ing line density of 400 L/mm, 800 L/mm, 1200 L/mm and  
 111 3600L/mm respectively. These gratings covering overlapping  
 112 energy ranges for flexible resolution-light intensity trade-offs.  
 113 A pre-mirror (M2) with dual Au/Ni coatings optimizes reflec-  
 114 tivity across energies, while its single-axis rotation mecha-  
 115 nism ensures precise grating alignment. For this purpose, the  
 116 pre-mirror undergoes a combination of translation and rota-  
 117 tion to ensure the grating illuminated at the correct angle of  
 118 incidence, maintaining the beam's focus at the exit slit. This  
 119 simultaneous translation and rotation are efficiently achieved

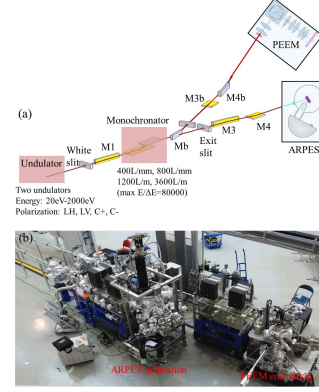


Fig. 1. (a) The optical layout and (b) the outside hutch site scene of the Dreamline beamline.

120 through a single rotation mechanism [32]. For the two distinct  
 121 reflective coatings Au and Ni (arranged side-by-side), the Ni  
 122 coating is used with the LEG and MEG, while the Au coating  
 123 is reserved for the HEG and VEGs, optimizing performance  
 124 across different energy ranges.

125 At the downstream side of PGM, the beamline split into  
 126 two branches for ARPES and PEEM. They operate in a time-  
 127 shared mode, achieved by switching the plane mirror Mb.  
 128 Two Kirkpatrick-Baez (KB) systems[33] then direct beams  
 129 to ARPES and PEEM endstations (Fig. 1b). For ARPES, el-  
 130 liptical cylindrical mirrors M3/M4 refocus the beam verti-  
 131 cally/horizontally after monochromatization. The PEEM branch  
 132 employs parallel optics through KB mirrors M3b/M4b, main-  
 133 taining spatial integrity for nanoscale imaging. All optical  
 134 components incorporate active thermal stabilization to coun-  
 135 teract thermal deformation, ensuring sub- $\mu m$  beam stability  
 136 critical for high-resolution measurements.

137 The performance of a state-of-the-art ARPES system  
 138 hinges critically on energy and angular resolutions, which  
 139 are directly determined by optical design and motion/ther-  
 140 mal stability treatment. To achieve the high energy resolution  
 141 goal of Dreamline, the beamline integrates several key inno-  
 142 vations: (1) Online thermal deformation correction mitigates  
 143 mirror distortions caused by high-power loads, improving en-  
 144 ergy resolution performance; (2) Hybrid focusing geometry  
 145 combines vertical dispersion with horizontal refocusing capa-  
 146 bilities, enhancing angular resolution precision; and (3) Ad-  
 147 vanced optical alignment protocols enable seamless integra-  
 148 tion of beam steering, stability control, and calibration proce-  
 149 dures. These systematic optimizations collectively establish  
 150 a new benchmark for resolving subtle electronic structures in  
 151 quantum materials, as demonstrated by the beamline's exper-  
 152 imental achievements in complex material studies.

## 153 III. OPTIMIZED BEAMLINE FOR HIGH ENERGY 154 RESOLUTION

155 To achieve the ultra-high resolution of the Dreamline, var-  
 156 ious aspects were considered during the design and construc-  
 157 tion of the beamline, including reducing system aberrations,

correcting thermal deformation through CFF optimization of the monochromator, controlling the temperature stability of the monochromator, and minimizing monochromator vibrations.

### 3.1 Reducing System Aberrations to Enhance Beamline Resolution

The energy resolution of the beamline is primarily determined by the following five key factors: the characteristics of the light source, the size of the exit slit, the meridional surface error of the grating, the meridional surface error of the plane mirror, and the aberrations of the entire optical system, as specifically expressed by Equation 1:

$$\Delta E_{\text{beamline}} = \sqrt{\Delta E_{\text{light}}^2 + \Delta E_{\text{pm}}^2 + \Delta E_{\text{grating}}^2 + \Delta E_{\text{slit}}^2 + \Delta E_{\text{aberration}}^2}$$

Among the factors influencing the energy resolution of the beamline, the energy broadening of the light source ( $\Delta E_{\text{light}}$ ) is primarily determined by intrinsic parameters such as the source emittance. The contributions from the plane mirror ( $\Delta E_{\text{pm}}$ ) and the monochromator grating ( $\Delta E_{\text{grating}}$ ) depend on the surface fabrication accuracy of the optical components. Specifically, the surface error of the plane mirror is  $0.2 \mu\text{mrad}$ , while that of the grating ranges from  $0.1$  to  $0.2 \mu\text{mrad}$ . The energy broadening contribution from the exit slit ( $\Delta E_{\text{slit}}$ ) is of the same order of magnitude as that of the light source. Notably, since the aberration of the plane mirror is zero, the resolution of the entire beamline is mainly determined by the aberration characteristics of the monochromator grating. It is particularly important to emphasize that the impact of aberrations on resolution exhibits spatial dependence, with its influence significantly increasing as the beam deviates further from the center of the mirror surface.

To achieve high energy resolution in the beamline, effectively suppressing optical aberrations is crucial. In the design of the Dreamline beamline, an innovative single focusing element scheme—namely, the VLS grating of the monochromator—was adopted as the sole optical element upstream of the exit slit. By precisely optimizing the geometric parameters of the VLS grating, the system aberrations can be reduced to near-zero levels. Specifically, at a specific optimized energy point (e.g.,  $1000 \text{ eV}$ ), the third-order aberration coefficient ( $F_{30}$ ) and the fourth-order aberration coefficient ( $F_{40}$ ) can both be nullified by appropriately selecting the VLS grating parameters  $b_3$  and  $b_4$ . Although  $F_{30}$  and  $F_{40}$  are not zero at non-optimized energy points, their values remain extremely low, ensuring high-resolution performance across the entire working energy range.

### 3.2 Thermal Deformation Correction to Improve Beamline Energy Resolution

Synchrotron radiation undulator sources are characterized by high energy density and broad spectrum properties. The upstream optical elements of the monochromator, due to absorbing a significant amount of heat, undergo thermal deformation, which severely affects the performance of the beamline. Below, we analyze how the thermal deformation, approximated as convex mirrors for M1 and M2, impacts the focusing conditions of the variable line spacing grating in the monochromator.

Since M1 is vertically mounted and the monochromator's plane mirror M2 is horizontally mounted, the thermal deformation in the meridional direction of M1 and the sagittal direction of M2 mainly affects the horizontal focusing, with no significant impact on the energy resolution. Based on theoretical simulation results,[20] the thermal deformation on the surface of the M1 plane mirror, which uses microchannel internal water cooling, can be equivalently considered as a convex mirror with a curvature radius of  $2.9 \times 10^5 \text{ m}$ . This deformation increases the horizontal divergence angle of the light source, leading to an approximately  $0.5\%$  increase in the object distance of the KB mirror. This change can be corrected by adjusting the grazing incidence angle of the KB mirror.

Through ANSYS numerical simulations combined with SHADOW tracing analysis, it was found that the thermal deformation in the sagittal direction of M1 can be approximated as a cylindrical mirror, and its impact on energy resolution is negligible. For the monochromator's plane mirror M2, which also uses microchannel internal water cooling, the thermal deformation equivalent curvature radius is  $6000 \text{ m}$ . This deformation alters the object distance of the grating, affecting the focusing conditions at the exit slit and leading to a decrease in energy resolution. To address this issue, this study employs a VLS grating with non-parallel light incidence for vertical beam focusing, optimizing the Cff value to adjust the focus point. Simulation results show that when the Cff value is increased from  $7$  to  $7.363$ , [20] the beamline's energy resolution significantly improves, effectively compensating for the performance degradation caused by thermal deformation. Ultimately, the optimal performance indicators for beamline spot size and resolution were achieved, with the experimental station measuring a best resolution of over  $50000@1000\text{eV}$ . This research provides an effective solution for compensating thermal deformation in synchrotron radiation beamlines, offering significant theoretical and practical implications for enhancing beamline performance.

### 3.3 Impact of Temperature Fluctuations on Beamline Energy Resolution

Theoretical analysis of the effect of temperature fluctuations on monochromator performance indicates that changes in ambient temperature cause a relative height difference between the front and rear support legs of the monochromator, leading to a rotation of the entire monochromator and ultimately resulting in beam energy drift. Since the temperature change process is relatively slow, this effect primarily manifests as a systematic shift in energy values, without significantly affecting the energy resolution. The structural parameters of the Dreamline monochromator are as follows: the overall height of the monochromator  $H = 1.3 \text{ m}$ , the distance between the front and rear support legs  $L = 1 \text{ m}$ , and the support material is stainless steel (linear thermal expansion coefficient

$$\alpha = 1.5 \times 10^{-5} \text{ K}^{-1} \quad (1)$$

. When there is a temperature difference  $\Delta T = 0.1 \text{ K}$  between the front and rear support legs, the rotation angle  $\theta$  can be calculated using the following formula:

$$\begin{aligned}
\theta &\approx \arctan(\alpha \cdot \Delta T \cdot H/L) \\
&= \arctan(1.5 \times 10^{-5} \times 0.1 \times 1.3) \\
&= 1.95 \times 10^{-6} \text{ rad}
\end{aligned} \tag{2}$$

This minute rotation angle will cause a change in the beam path, leading to a systematic drift in energy values. In practical operation, it is necessary to establish a temperature monitoring system and develop corresponding compensation algorithms to eliminate the interference of temperature fluctuations on experimental results.

For a 3600 L/mm VEG grating, when ambient temperature fluctuations cause a temperature difference of 0.1 K, it results in an energy drift of 35.8 meV@1000 eV. This value exceeds the system's resolution at 1000 eV (20 meV), making it a non-negligible source of systematic error. To effectively address this issue, this study proposes a material optimization solution: replacing the stainless steel support material of the monochromator with granite, which has superior thermal stability ( $\alpha = 0.3 \times 10^{-5} K^{-1}$ ). Theoretical calculations after material optimization show that under the same temperature difference condition ( $\Delta T = 0.1$  K), the energy drift caused by granite supports is reduced to 7.2 meV@1000 eV, which is below the system's energy resolution and meets experimental requirements. Based on these research results, by constructing a constant-temperature enclosure to control the temperature difference between the front and rear support legs within 0.1 K, combined with an active temperature control system, the impact of temperature fluctuations on system performance is further reduced.

This optimization solution not only effectively resolves the energy drift issue but also provides important references for the thermal stability design of high-precision grating systems. Through the synergistic effect of material optimization and temperature control, the system can maintain an energy resolution better than 20 meV at 1000 eV, meeting the requirements for precision experimental measurements.

### 3.4 Impact of Vibration on Beamline Energy Resolution

The vibration level of the SSRF foundation is  $0.2 \mu m$  (RMS). Under the most unfavorable conditions, a vertical relative displacement of  $0.4 \mu m$  may occur between the front and rear support legs of the monochromator, resulting in an angular change of  $\delta = 0.4 \mu m / 1 \text{ m} = 0.4 \mu rad$ . By analogy with the calculation method for the effect of temperature on energy drift, we systematically analyzed the relative energy drift caused by vibration, with detailed results shown in Table S1 (supporting information).

The vibration effect is most significant for the VEG grating, causing a reduction in energy resolution of approximately 10,000 at 1000 eV, while the performance changes for other types of gratings are relatively smaller. It should be noted that the above calculations are based on the most extreme estimation, assuming a maximum vertical relative displacement of  $0.4 \mu m$  between the front and rear support legs of the monochromator. In reality, due to the correlation between the vibrations of the front and rear support legs, the actual vertical relative displacement should be smaller than

this theoretical value. Nevertheless, to ensure optimal energy resolution, an independent foundation was designed for the monochromator system in the construction of the Dreamline beamline, effectively isolating environmental vibrations. The foundation uses granite material with a low thermal expansion coefficient, simultaneously reducing the impact of temperature fluctuations and vibrations. This improvement scheme provides reliable technical support for enhancing beamline resolution.

## IV. BEAMLINE PERFORMANCE

The performance of the beamline including energy resolution, photon flux, energy range, and spot size at sample position is thoroughly evaluated with the suitable exit slit aperture.

### 4.1 Energy resolution measured by beamline ionization chamber

The primary factors influencing the energy resolution within a beamline can be classified into five key components: the dimensions of the light source, the geometry of the exit slit, the meridional profile accuracy of the grating, the meridional profile precision of the plane mirror, and the overall aberrations along the optical path. Notably, the aberrations introduced by the plane mirror in a grating monochromator are negligible, with the primary source of aberrations stemming exclusively from the grating. Through meticulous calculations, it has been determined that the effect of these aberrations on the energy resolution is minimal and can, therefore, be disregarded. In the realm of grating systems, the most crucial determinant of energy resolution is the size of the light source, closely followed by the influence of the exit slit (particularly in low-energy gratings, or LEGs, and medium-energy gratings, or MEGs) and the error in the grating's profile.

To precisely evaluate the beamline resolution, an ionization chamber was strategically positioned downstream of the exit slit, serving as the cornerstone for measuring the inner shell excitation spectra of standard gases, as expressed in our previous report.[34] This chamber consists of a vacuum cavity, a leak valve equipped with a gas inlet, an MCP (Microchannel Plate) detector, and a nuclear electronics system (ORTEC 584/996) which is responsible for amplifying and counting ion pulses. A key advantage of this setup is its capability to perform measurements under extremely low working pressures, thereby significantly reducing the influence of collision broadening on the results. In our experimental endeavors, we recorded spectra at a gas pressure of  $1 \times 10^{-6}$  Torr, using a white slit aperture with dimensions of  $400 \mu m \times 1000 \mu m$ , and an exit slit aperture varying from  $20 \mu m$  to  $250 \mu m$ . The observed spectrum peak displayed a distinct Voigt profile, which is fundamentally a convolution of a Lorentzian-broadened peak, indicative of natural lifetime broadening with a linewidth of  $\Delta L$ , and the beamline's instrumental resolution, modeled as a Gaussian function characterized by a width of  $\Delta G$ . By using the known Lorentz broadening of the intrinsic Ne gas absorption, specifically

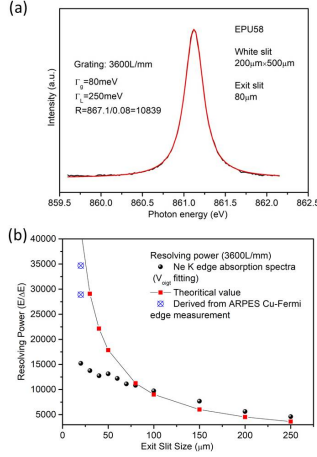


Fig. 2. Ion yield spectra measured using the 3600 lines/mm grating. (a) Excitation spectra for Ne gas at the Ne K-edge at 867.1 eV, with an exit slit opening of 80 μm. The resolving power is 10839, determined from Voigt fitting of the 1s → 3p transition peak. (b) Theoretical and Voigt fitting values of beamline resolving power for different exit slit openings.

$\Delta E_{Ne-K}=250$  meV, as a benchmark, we were able to deduce  $\Delta G$  as a reliable indicator of the beamline's energy resolution. [35]

The core excitations in gas-phase Ne near the Ne-K threshold have been investigated using MCP measurements in an ionization chamber equipped with a 3600 L/mm grating. The Ne K absorption-edge transition to the Rydberg levels 1s → 3p at  $h\nu = 867.1$  eV was observed in Figure 3a, in order to characterize the energy resolution. The peak was simulated using a Voigt profile, assuming a Lorentzian linewidth of  $L = 250$  meV, with a Gaussian width of  $\Delta G = 80$  meV deconvolved from the beamline resolution. This yields a resolving power ( $E/\Delta E$ ) of 10839, corresponding to an energy resolution ( $\Delta E$ ) of 80 meV, under the condition of an 80 μm exit slit. Figure 3b presents the 1s-3p core-excitation resonances of gas-phase Ne recorded using various exit slit apertures. The theoretical value of the beamline resolution was obtained via SHADOW ray-tracing, as previously reported in our work. Unfortunately, as the exit slit size decreases, the intrinsic 1s → 3p peak width approaches the value of the Lorentzian linewidth, leading to significant errors in the Voigt fitting. When the exit slit is smaller than 80 μm, an unambiguous fit of the 1s-3p resonance at 867.1 eV using a Lorentzian line convolved with a Gaussian profile becomes challenging, with fitting uncertainty coming close to the profile width. Consequently, it becomes unreliable to determine the ultimate resolution as evident in Figure 3b by the further deviation of measured resolving power from theoretical prediction.

## 4.2 Energy resolution by ARPES

Given the inaccuracy of the Voigt fitting method for measuring the absorption spectrum of rare gases through an ionization chamber in determining the energy resolution of the beamline in ultra-high regime, we have opted to use an

ARPES experimental station through measuring the Fermi distribution function, which subsequently allows us to accurately assess high resolution. For energy resolution purposes, the comprehensive resolution of the ARPES system can be mathematically expressed in Formula 2[36]:

$$\Delta E_{\text{total}} = \sqrt{\Delta E_{\text{light}}^2 + \Delta E_{\text{analyzer}}^2 + \Delta E_{\text{noise}}^2 + \Delta E_{\text{other}}^2 + \Delta E_T^2} \quad (3)$$

$\Delta E_{\text{light}}$  denotes the energy broadening inherent to the light source. In the case of a helium lamp, this broadening is exceptionally narrow, measuring less than 1 meV. Conversely, for synchrotron radiation light, the extent of energy broadening is predominantly governed by various factors, notably including the undulator light source and the grating. As a general rule, an increase in photon energy is accompanied by a corresponding increase in the broadening.

$\Delta E_{\text{analyzer}}$  signifies the energy resolution capability of the ARPES analyzer. This resolution is primarily influenced by three key factors: the pass energy ( $E_p$ ), the width of the analyzer's slit, and its acceptance angle. As a general rule, reducing either the pass energy, the slit width, or the acceptance angle results in an enhancement of the analyzer's resolution. However, this is achieved at the cost of a decreased photocurrent intensity passing through the slit within a given time frame, ultimately leading to a weaker signal. Consequently, to optimize the signal-to-noise ratio in experiments, a delicate balance must be found between maximizing resolution and ensuring sufficient photocurrent intensity, thereby selecting a configuration that provides the best overall performance.

$\Delta E_{\text{noise}}$  represents the broadening caused by noise, which should be minimized as much as possible. For this purpose, the equipment should be properly grounded and the vibrations should be reduced.

$\Delta E_{\text{other}}$  represents the broadening caused by a variety of factors, including spot jitter, spatial magnetic fields, and charge effects, all of which should be minimized as much as possible. As a practical example, maintaining various optical components at stable temperatures and pressures serves to effectively prevent spot jitter.

$\Delta E_T$  embodies the broadening effect attributable to temperature variations. In pursuit of ultra-high energy resolution, experiments are typically conducted under exceedingly low temperatures, aiming to mitigate the impact of temperature broadening and thereby enhance the precision of the measurements. The first four factors can be collectively designated as the instrumental resolution,

$\Delta E_{\text{system}}$ , of the ARPES experimental system. The total and instrumental resolutions of the actual system are characterized by measuring the characteristic width of the Fermi edge of gold or copper. In the case of the Fermi distribution function, there is no discernible peak-shaped structure, and thus the half-height width cannot be adopted as the characteristic width through a Gaussian distribution fit. Instead, the energy range corresponding to a Fermi distribution value from 0.9 to 0.1 of its maximum is typically taken as the characteristic width. Based on this definition, we have:



$$f(E_1) = \frac{1}{e^{(E_1 - E_F)/(k_B T)} + 1} = 0.9 \quad (4)$$

$$f(E_2) = \frac{1}{e^{(E_2 - E_F)/(k_B T)} + 1} = 0.1 \quad (5)$$

the characteristic width can be expressed in formula 3:

$$\Delta E_{fit} = 2 \ln 9 \cdot k_B T \quad (6)$$

Herein,  $\Delta E_{fit}$  denotes the fitted characteristic width, while  $k_B$  represents the Boltzmann constant, and  $T$  signifies the sample temperature. As clearly demonstrated by the previously mentioned formula, the characteristic width of the Fermi function exhibits a linear dependence on temperature. By applying the Fermi distribution function to fit the Energy Distribution Curve (EDC) of the sample, we can ascertain the fitted temperature,  $T_{fit}$ . Subsequently, the aforementioned formula is applied to compute the characteristic width,  $\Delta E_{fit}$ , of the Fermi distribution function, which acts as a measure of the system's total measurement resolution. To isolate the instrument resolution, the characteristic width is then adjusted by subtracting the intrinsic width of the Fermi distribution function at the experimental temperature. The instrument's resolution can then be approximated using the formula outlined in formula 4:

$$\Delta E_{system} = \sqrt{\Delta E_{fit}^2 - \Delta E_T^2} \quad (7)$$

To determine the energy resolution of a synchrotron radiation beamline, it is essential to employ the helium lamp integrated within the ARPES system as a standard for measuring its ultimate resolution. Under identical experimental conditions, we compare the resolutions attained through measurements utilizing both the helium lamp and synchrotron radiation. Given the negligible energy broadening of the helium lamp, which is merely 0.4 meV at 21.2 eV, its contribution to broadening can be disregarded. Thus, the disparity between the two measurements is solely attributable to the energy broadening of the synchrotron radiation, which consequently represents the resolution of the synchrotron radiation beamline.

$$\Delta E_{beam} = \sqrt{\Delta E_{total(beam)}^2 - \Delta E_{total(He)}^2} \quad (8)$$

By conducting ARPES testing on Cu with a helium lamp as the light source, under the conditions of a 13K temperature and a 0.3mm analyzer slit setting, the Fermi edge of the Cu surface was measured, yielding an analyzer resolution of 26.4 meV. Similarly, utilizing a monochromator grating with a ruling density of 3600 lines per millimeter (L/mm), the Fermi edge of the Cu surface was measured again, this time with 867 eV synchrotron radiation, resulting in a system resolution of 22 meV. However, based on further analysis and the provided formula, the resolution of the Dreamline beamline

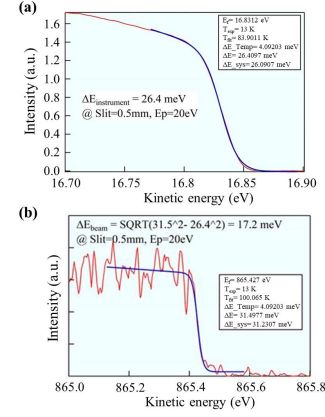


Fig. 3. The resolution test results for the Dreamline are presented as follows: (a) By measuring the Fermi edge of the Cu surface using a helium lamp as the light source, under the conditions of a temperature of 13K and an analyzer slit setting of 0.3mm, the analyzer resolution was determined to be 26.4 meV. (b) Utilizing 867 eV synchrotron radiation to measure the Fermi edge of the Cu surface, the beamline resolution was calculated to be 17.2 meV. The resolving power was derived as  $867/0.0172$ , resulting in a value of 50,400@867eV.

specifically is determined to be 17.2 meV, corresponding to an energy resolving power of 50,400 at 867 eV.

#### 4.3 Photon flux measurement

The photon flux at the anticipated sample position was determined using an AXUV100G photodiode, whose photocurrent, induced by the incident beam, is linearly proportional to the flux. The photon flux can be calculated based on the photoelectric conversion efficiency of the photodiode, as outlined in formula 6[37]:

$$\text{Flux} = I \times 3.66 \times 250 / (e \times I_{BC} \times \Delta E_{beam} \times 10000) \quad (\text{formula 6})$$

Where  $I$  is the photocurrent (A) recorded by the photodiode at the sample position,  $e$  is the electron charge of  $1.6 \times 10^{-19}$  C,  $E_{beam}$  refers to the energy broadening (in eV) at the gas absorption edge, and  $I_{BC}$  stands for the ring current (mA) during flux measurement. Since the beamline flux is inherently linked to both the beamline bandwidth and the energy value, the flux measurement corresponds to an experimental condition of a 0.01% bandwidth. The beamline bandwidth is adjustable via the monochromator slit size, while energy calibration is achieved using a gas ionization chamber. Through rigorous testing, the Dreamline beamline has demonstrated the capability to perform full-energy-range flux measurements under a  $4\sigma$  opening of the white light slit for the double undulator. This includes measurements utilizing corresponding gratings under varying light polarization conditions (LH for horizontal polarization and C for circular polarization). By selecting the appropriate grating, this beamline can guarantee a flux exceeding 1012 phs/s/0.01%BW below 800 eV and a flux exceeding  $10^{11}$  phs/s/0.01%BW across the entire energy range (20-2000 eV).

#### 4.4 Beam spot sizes at the ARPES sample

An X-ray beam position monitor (BPM) system is in-

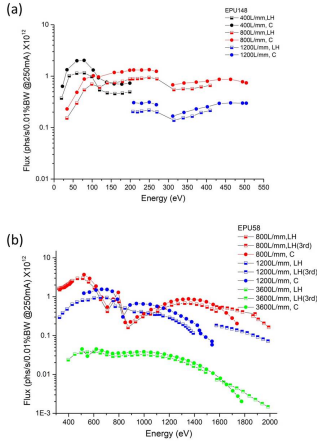


Fig. 4. The photocurrent was measured during an energy scan centered at 244 eV of the EPU fundamental, using a grating with a line density of 300 L/mm. The measurement was conducted under a ring current of 200 mA, with a white light slit opening of  $1000 \mu\text{m} \times 3200 \mu\text{m}$  and an exit slit opening of  $40 \mu\text{m}$ . (a) LEID, using 400L, 800L, 1200L under LH/C polarization; (b) HEID using 800L/mm, 1200L/mm, 3600L/mm under LH/C polarization.

stalled at the ARPES endstation and is ready to measure the spot sizes at any time. This system comprises a bottom-mounted manipulator in the main chamber, configured with a 100mm tungsten wire and a YAG:Ce scintillator, as well as an AXUV100G photodiode mounted downstream. The YAG:Ce scintillator is used to locate the X-ray beam position, while the photodiode measures the photon intensity of the direct soft X-ray beam.

The BPM is driven by stepper motors to scan across the beam spot at the intended sample position, resulting in a step change in the intensity of the photocurrent before and after shading. To obtain the spot profile in the horizontal or vertical direction, the step signal of the recorded photocurrent is differentiated (first derivative), and the spot size is derived from its full width at half maximum (FWHM) value. In our measurements, these scans were performed at approximately 100eV, using a white slit aperture of  $1000 \mu\text{m} \times 3000 \mu\text{m}$  and an exit slit aperture of  $50 \mu\text{m}$ . The measured beam spot size at the ARPES endstation is  $H:60 \mu\text{m} \times V:30 \mu\text{m}$  (see supporting information Fig.S1). The vertical size of the beam spot at the sample is a crucial factor in determining the energy resolution of the beam, which is influenced by the exit slit. The measured spot size in the vertical direction with varying exit sizes is shown in Fig. 5c, which is in accordance with the theoretical values.

## V. APPLICATIONS TO MATERIALS

The coexistence of a near Fermi Energy ( $E_F$ ) flat band and a Van Hove singularity in a two-phase superconductor was meticulously investigated using ARPES with high incident energy.[38] In correlated electron systems, the intricate interplay between charge, lattice, spin, and orbital de-

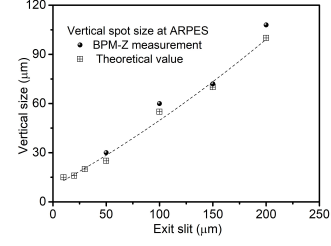


Fig. 5. Beam spot size measurements at the ARPES sample position. Derived spot sizes are presented along with the calculated and theoretical values of spot size in the vertical direction for different exit slit apertures, respectively. All measurements were carried out at 100eV using varying exit slit apertures.

grees of freedom fosters the emergence of multiple orders, which often coexist on similar energy scales, temperatures, or timescales. Unraveling and manipulating these diverse orders has remained a cornerstone in the realm of condensed matter physics. Among these, a pivotal aspect revolves around the intricate electronic structure proximal to the Fermi energy.

The Van Hove singularity (VHS), notably identified by its extrema and saddle points within the band structure, stands as a prominent source of significant density of states (DOS) in low-dimensional systems. Furthermore, it emerges as a pivotal player in orchestrating the intricate interplay among various orders, such as superconductivity, spin-density waves, and charge-density waves. Here, we present the first comprehensive band structure report, derived from an innovative combination of bulk-sensitive soft-x-ray and resonant VUV-ARPES techniques. Remarkably, our analysis uncovers a VHS residing at the X point of the Brillouin zone edge, which exhibits a unique hybridization with the  $4f_{5/2}$  bands in close proximity to the Fermi energy. This discovery not only sheds light on the fundamental nature of the multifaceted phases present in  $\text{CeRh}_2\text{As}_2$  but also paves the way for groundbreaking explorations into the exotic phenomena arising from the hybridization of f-electrons with VHS features in many-body systems. The study thus opens up new avenues for understanding and harnessing these novel properties, with potential implications across various fields of condensed matter physics.

In Figure 6, we present ARPES intensity plots spanning a broad photon-energy range from 95 to 205 eV. Distinctively, the presence of two flat bands located approximately at -0.25 eV below the Fermi level is consistently observed across all panels, providing unequivocal evidence for the existence of the  $4f_{7/2}$  and  $4f_{5/2}$  flat bands. Notably, these measured flat bands exhibit a pronounced enhancement in spectral intensity at the intersection points with the conduction bands (Figure 6c), indicative of c-f hybridization. A comprehensive investigation into the band structure of  $\text{CeRh}_2\text{As}_2$  is conducted utilizing bulk-sensitive soft X-ray ARPES. The high-resolution soft-x-ray ARPES data presented here offer valuable insights into the intricate phase diagram of  $\text{CeRh}_2\text{As}_2$ , which is crucial for unraveling the intricate entanglement of hybridized electrons in various symmetry-broken phases. This study represents a significant step forward in understanding the novel

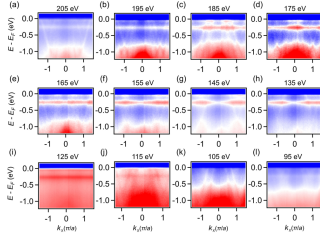


Fig. 6. Heavy 4f-electron flat band along  $\Gamma^- - X^-$  at 20 K by wide-range photon-energy-dependent ARPES measurements with LH F12:2 polarization, measured by the soft X-ray ARPES in dreamline. [39]

properties of this fascinating material.

## VI. SUMMARY

The ultra-high energy resolution soft X-ray beamline, constructed at the SSRF, is dedicated to ARPES and PEEM experimental applications. The employment of two EPU demonstrates a broad working energy range spanning from

20 to 2000 eV. To achieve individual high energy resolutions, the beamline is optimized with a plane-grating monochromator that incorporates four VLS gratings, enabling the acquisition of either exceptionally high flux or resolving power. A remarkable resolving power of 50,400 has been attained at 867.1 eV through the use of a high-line density grating, further enhanced by the thermal correction capabilities inherent in this monochromator design. Additionally, the Dreamline beamline has successfully conducted full-energy-range flux measurements for the double undulator, utilizing a  $4\sigma$  opening of the white light slit. These measurements encompass data collected using the corresponding gratings under varying light polarization conditions. Notably, below 800 eV, by selecting the appropriate grating, this beamline guarantees a flux exceeding  $10^{12}$  photons/second/0.01% bandwidth, while maintaining a flux above  $10^{11}$  photons/second/0.01% bandwidth across the entire 20-2000 eV energy range. The outstanding performance in terms of energy resolution, flux, and wide energy coverage significantly bolsters research endeavors in quantum-related materials, enabling scientists to delve deeper into their fundamental properties and behaviors.

## VII. BIBLIOGRAPHY

- [1] H. Zhong, *et al.*, Revealing the two-dimensional electronic structure and anisotropic superconductivity in a natural van der Waals superlattice (PbSe)<sub>1.14</sub>NbSe<sub>2</sub>. *Physical Review Materials*, **7**: L041801. (2023). DOI:10.1103/PhysRevMaterials.7.L041801
- [2] W. Fan, *et al.*, Discovery of  $C_2$  rotation anomaly in topological crystalline insulator SrPb. *Nature Communications*, **12**: 2052. (2021). DOI:10.1038/s41467-021-22350-6
- [3] Z. Wu, *et al.*, Revealing the Heavy Quasiparticles in the Heavy-Fermion Superconductor CeCu<sub>2</sub>Si<sub>2</sub>. *Physical Review Letters*, **127**: 067002. (2021). DOI:10.1103/PhysRevLett.127.067002
- [4] Y.-P. Zhu, *et al.*, Observation of plaid-like spin splitting in a noncoplanar antiferromagnet. *Nature*, **626**: 523-528. (2024). DOI:10.1038/s41586-024-07023-w
- [5] C. Y. Tang, *et al.*, Suppression of antiferromagnetic order in the electron-doped cuprate T'-La<sub>2-x</sub>Ce<sub>x</sub>CuO<sub>4±δ</sub>. *Physical Review B*, **104**: 155125. (2021). DOI:10.1103/PhysRevB.104.155125
- [6] H. Yang, *et al.*, Visualizing electronic structures of quantum materials by angle-resolved photoemission spectroscopy. *Nature Reviews Materials*, **3**: 341-353. (2018). DOI:10.1038/s41578-018-0047-2
- [7] K. Y. Arutyunov, *et al.*, Superconducting insulators and localization of Cooper pairs. *Communications Physics*, **4**: 146. (2021). DOI:10.1038/s42005-021-00648-7
- [8] B. Lv, T. Qian, H. Ding, Angle-resolved photoemission spectroscopy and its application to topological materials. *Nature Reviews Physics*, **1**: 609-626. (2019). DOI:10.1038/s42254-019-0088-5
- [9] V. A. Posey, *et al.*, Two-dimensional heavy fermions in the van der Waals metal CeSiI. *Nature*, **625**: 483-488. (2024). DOI:10.1038/s41586-023-06868-x
- [10] B. A. Bernevig, C. Felser, H. Beidenkopf, Progress and prospects in magnetic topological materials. *Nature*, **603**: 41-51. (2022). DOI:10.1038/s41586-021-04105-x
- [11] H. Zhang, *et al.*, Angle-resolved photoemission spectroscopy. *Nature Reviews Methods Primers*, **2**: 54. (2022). DOI:10.1038/s43586-022-00133-7
- [12] J. Feng, A. Scholl, in *Springer Handbook of Microscopy* (eds P. W. Hawkes, J. C. H. Spence), 537-564. Springer International Publishing. (2019).
- [13] A. Damascelli, Z. Hussain, Z.-X. Shen, Angle-resolved photoemission studies of the cuprate superconductors. *Reviews of Modern Physics*, **75**: 473-541. (2003). DOI:10.1103/RevModPhys.75.473
- [14] S. Souma, *et al.*, Ultrahigh-resolution spin-resolved photoemission spectrometer with a mini Mott detector. *Review of Scientific Instruments*, **81**: 095101. (2010). DOI:10.1063/1.3480542
- [15] M. Z. Hasan, C. L. Kane, Colloquium: Topological insulators. *Reviews of Modern Physics*, **82**: 3045-3067. (2010). DOI:10.1103/RevModPhys.82.3045
- [16] P. Richard, *et al.*, Observation of momentum space semi-localization in Si-doped  $\beta$ -Ga<sub>2</sub>O<sub>3</sub>. *Applied Physics Letters*, **101**: 041901. (2012). DOI:10.1063/1.4769109
- [17] M. Kobayashi, *et al.*, Digging up bulk band dispersion buried under a passivation layer. *Applied Physics Letters*, **101**: 251603. (2012). DOI:10.1063/1.4770289
- [18] M. J. Prieto, T. Schmidt, LEEM and PEEM as Probing Tools to Address Questions in Catalysis. *Catalysis Letters*, **147**: 2487-2497. (2017). DOI:10.1007/s10562-017-2162-x
- [19] V. N. Strocov, *et al.*, High-resolution soft X-ray beamline ADDRESS at the Swiss Light Source for resonant inelastic X-ray scattering and angle-resolved photoelectron spec-



- 713 troscopies. Journal of Synchrotron Radiation, **17**: 631-643. (2010). DOI:10.1107/S0909049510019862
- 714 [20] L. Xue, *et al.*, Design of an ultrahigh-energy-resolution and wide-energy-range soft X-ray beamline. Journal of Synchrotron Radiation, **21**: 273-279. (2014). DOI:10.1107/S1600577513029093
- 715 [21] B. Q. Lv, *et al.*, Experimental Discovery of Weyl Semimetal TaAs. Physical Review X, **5**: 031013. (2015). DOI:10.1103/PhysRevX.5.031013
- 716 [22] B. Q. Lv, *et al.*, Observation of three-component fermions in the topological semimetal molybdenum phosphide. Nature, **546**: 627-631. (2017). DOI:10.1038/nature22390
- 717 [23] Z. Rao, *et al.*, Observation of unconventional chiral fermions with long Fermi arcs in CoSi. Nature, **567**: 496-499. (2019). DOI:10.1038/s41586-019-1031-8
- 718 [24] K. Liu, *et al.*, BL02U1: the relocated macromolecular crystallography beamline at the Shanghai Synchrotron Radiation Facility. Nuclear Science and Techniques, **34**: 193. (2023). DOI:10.1007/s41365-023-01348-3
- 719 [25] Y. Tie-Ying, *et al.*, Introduction of the X-ray diffraction beamline of SSRF. Nuclear Science and Techniques, **26**: 020101. (2015). DOI:10.13538/j.1001-8042/nst.26.020101
- 720 [26] Z. Zhao, H. Xu.
- 721 [27] Z. P. Sun, *et al.*, Performance of the BL03U beamline at SSRF. Journal of Synchrotron Radiation, **27**: 1388-1394. (2020). DOI:10.1107/S1600577520008310
- 722 [28] F.-Y. Zhu, *et al.*, Spatial- and spin-resolution ARPES and magnetism beamline at SSRF. Nuclear Science and Techniques, **35**: 130. (2024). DOI:10.1007/s41365-024-01484-4
- 723 [29] R.-Z. Tai, Z.-T. Zhao, Overview of SSRF phase-II beamlines. Nuclear Science and Techniques, **35**: 137. (2024). DOI:10.1007/s41365-024-01487-1
- 724 [30] X. P. Wang, *et al.*, Orbital characters determined from Fermi surface intensity patterns using angle-resolved photoemission spectroscopy. Physical Review B, **85**: 214518. (2012). DOI:10.1103/PhysRevB.85.214518
- 725 [31] R. Reininger, The in-focus variable line spacing plane grating monochromator. Nuclear Instruments and Methods in Physics Research Section A: Accelerators, Spectrometers, Detectors and Associated Equipment, **649**: 139-143. (2011). DOI:10.1016/j.nima.2010.12.162
- 726 [32] F. Riemer, R. Torge, Bessy SX 700 UHV monochromator: Design features and kinematic concept. Nuclear Instruments and Methods in Physics Research, **208**: 313-314. (1983). DOI:10.1016/0167-5087(83)91141-9
- 727 [33] P. Kirkpatrick, A. V. Baez, Formation of Optical Images by X-Rays. Journal of the Optical Society of America, **38**: 766-774. (1948). DOI:10.1364/JOSA.38.000766
- 728 [34] J. Li, *et al.*, NUCLEAR TECHNIQUES, **39**: 050101. (2016). DOI:10.11889/j.0253-3219.2016.hjs.39.050101
- 729 [35] M. Domke, *et al.*, Performance of the high-resolution SX700/II monochromator. Review of Scientific Instruments, **63**: 80-89. (1992). DOI:10.1063/1.1142615
- 730 [36] H. Iwasawa, High-resolution angle-resolved photoemission spectroscopy and microscopy. Electronic Structure, **2**: 043001. (2020). DOI:10.1088/2516-1075/abb379
- 731 [37] X. Meng, *et al.*, Design and performance of bending-magnet beamline BL02B at the SSRF. Journal of Synchrotron Radiation, **26**: 543-550. (2019). DOI:10.1107/S1600577518018179
- 732 [38] T. Yoshida, M. Sigrist, Y. Yanase, Pair-density wave states through spin-orbit coupling in multilayer superconductors. Physical Review B, **86**: 134514. (2012). DOI:10.1103/PhysRevB.86.134514
- 733 [39] X. Chen, *et al.*, Coexistence of near- $E_F$  Flat Band and Van Hove Singularity in a Two-Phase Superconductor. Physical Review X, **14**: 021048. (2024). DOI:10.1103/PhysRevX.14.021048